



Cite this: *Green Chem.*, 2015, **17**, 3889

## Lactic acid production from hydroxyacetone on dual metal/base heterogeneous catalytic systems

Elise M. Albuquerque,<sup>a,b</sup> Luiz E. P. Borges<sup>b</sup> and Marco A. Fraga<sup>\*a,b</sup>

Oxidative aqueous-phase catalytic conversion of hydroxyacetone to lactic acid was investigated under mild and green reaction conditions. Dual metal/base catalyst systems were applied to replace the alkali hydroxide and address the separation requirements and corrosiveness issues usually involved in similar processes. Pt/Al<sub>2</sub>O<sub>3</sub> was taken as the supported metal catalyst while Mg–Al layered double hydroxides (LDH) and their derived 3D mixed oxides were exploited as basic solid catalysts. The anion embedded within the LDH interlamellar domain (nitrate or hydroxyl) and the LDH topology (lamellar or exfoliated 2D nanosheets) were also examined. Activity and chemoselectivity of the dual system were shown to be tailored by the morphology, topology and basicity of the base catalyst. Catalytic activity was up to five times higher by adding a heterogeneous base solid to the metal catalyst. Surface site distribution was also shown to be quite decisive to the catalyst performance; the proximity of metal and basic centres on the same surface rendered highly selective bifunctional catalysts. A remarkable 100% selectivity to lactic acid was reached and the undesired cascade oxidation of lactic to pyruvic acid was hindered.

Received 6th April 2015,  
Accepted 19th May 2015

DOI: 10.1039/c5gc00736d

www.rsc.org/greenchem

## Introduction

As a consequence of the ever-growing global concern about minimizing environmental impacts caused by the use of fossil fuel-derived products, much effort has been made focusing on the development of new technologies based on renewable sources. Those relying on processing sidestream compounds from the bioenergy industry are increasingly more interesting since they may make biofuels more cost-competitive by co-producing high added-value chemicals. Processes focused on glycerol transformation, a co-product of biodiesel production, match such approach. The continuous large availability of glycerol worldwide has been motivating its use as a green feedstock for the synthesis of many valuable compounds, particularly diols,<sup>1–3</sup> ethers<sup>4,5</sup> and carboxylic acids.<sup>6–11</sup>

Amongst the wide range of carboxylic acids, lactic acid comes up due to its large industrial use in different sectors, from the conventional ones (food and cosmetics) to solvents, chemical specialties and biodegradable green plastics. In this latter field of application, the upsurging market of poly(lactic acid) – PLA – stands out.

PLA is a biodegradable, compostable and biocompatible polymer, which enables its use in eco-friendly packages and

medical materials such as sutures, controlled drug delivery systems and orthopaedic implants.<sup>12,13</sup> Moreover, once disposed, PLA degradation releases CO<sub>2</sub> and water, affording a carbon neutral balance. All these advantages have boosted the demand of PLA and have consequently motivated the search for new competitive industrial processes to obtain lactic acid.

Lactic acid can be produced by several different routes such as the traditional biological process (fermentative),<sup>14,15</sup> chemical synthesis<sup>16,17</sup> and homogeneous<sup>10,11</sup> or heterogeneous<sup>18,19</sup> catalytic reactions.

The fermentative synthesis corresponds to approximately 90% of the worldwide production<sup>14</sup> and it is based on fermentation of sugars.<sup>15</sup> Despite its current industrial application, it is a complex process because the microorganisms used require suitable conditions for their growth, nutrients for its cultivation and, more importantly, the process is time consuming taking two to four days to accomplish profitable yields.<sup>20,21</sup>

Homogeneous catalyzed reactions make use of saccharides (cellulose, sucrose, fructose and glucose) as the major feedstocks and the process occurs in an aqueous medium with metal salts.<sup>22,23</sup> Transformation of glycerol to lactic acid with a large excess of inorganic hydroxides as homogeneous catalysts has also been reported.<sup>10,11</sup> However, high yields are only achieved under hydrothermal conditions; that is to say that severe conditions (temperature and pressure) are demanded in addition to the need of strong, aggressive hydroxides, which are neither recovered nor recycled. Consequently, the costs involved in these processes are expected to be quite high, discouraging their technological exploitation.

<sup>a</sup>Instituto Nacional de Tecnologia, Laboratório de Catálise, Av. Venezuela, 82/518, 20081-312 Rio de Janeiro, RJ, Brazil. E-mail: marco.fraga@int.gov.br

<sup>b</sup>Instituto Militar de Engenharia, Praça Gen. Tibúrcio 80, Praia Vermelha, Urca, 22290-270 Rio de Janeiro, RJ, Brazil

Alternatively, lactic acid can be obtained from single or multi-step conversion of glycerol<sup>24</sup> over heterogeneous catalytic systems. One-pot aerobic oxidation was reported over monometallic (Au, Pd and Pt) and bimetallic Au–Pt supported catalysts and selectivities as high as 85% were reached.<sup>24</sup> Pt rendered the more active monometallic catalyst but irrespective of the support, the presence of a soluble metal hydroxide (NaOH : glycerol = 4 : 1 molar ratio) was found to be mandatory. These results seemed to be conflicting with the widespread literature reporting glyceric acid as the main product from glycerol oxidation under alkaline conditions.<sup>25–30</sup> Nevertheless, it was claimed that competitive parallel reactions leading to either glyceric acid (*via* oxidative dehydrogenation and oxidation steps) or lactic acid (*via* oxidative dehydrogenation and intramolecular rearrangement steps) may occur and the adjustment of the reaction conditions may determine product distribution.

More recently, a biochemical–chemical two-step reaction approach was proposed in which glycerol could be bioconverted to dihydroxyacetone through microbiological oxidation, followed by its chemical rearrangement to lactic acid in alkaline medium.<sup>31</sup> For such a second reaction step, alkaline-earth metal hydroxides were exploited as catalysts, as an alternative to alkali hydroxides, due to their fairly low solubility, thus allowing mechanical separation. Lactic acid yields of around 60% were achieved by using Ca(OH)<sub>2</sub> and the formation of Ca<sup>2+</sup> chelates is suggested to drive the chemical conversion.<sup>31,32</sup> Alternatively, dihydroxyacetone can be converted to lactic acid over solid Lewis acid catalysts and yields varying from 30 to 100% were reached over boehmite  $\gamma$ -AlO(OH)<sup>33</sup> and Sn-containing MFI zeolite<sup>34</sup> as catalysts, respectively.

Other multi-step proposals for producing lactic acid from glycerol can be assembled. Initial glycerol conversion to 1,2-propanediol *via* hydrogenolysis<sup>35,36</sup> followed by diol selective oxidation<sup>18,37</sup> or glycerol dehydration to hydroxyacetone (acetol)<sup>38</sup> succeeded by oxidation/intramolecular rearrangement<sup>39</sup> are both feasible approaches.

In previous work, we have reported the chemoconversion of hydroxyacetone to lactic acid over Pt-supported catalyst in the presence of NaOH at atmospheric pressure.<sup>39</sup> Remarkable selectivities (>96%) were accomplished and the results pointed to the crucial role of controlling the reaction conditions to avoid further oxidation of lactic acid to pyruvic acid.

This study evaluates the oxidative aqueous-phase catalytic conversion of hydroxyacetone to lactic acid under milder and greener reaction conditions. Dual catalyst systems composed of a supported metal catalyst and layered double hydroxide-derived basic solids were applied to replace the alkali hydroxide and address the separation requirements and corrosiveness issues usually involved in similar processes.

## Experimental

### Catalyst synthesis

Layered double hydroxides (LDH) and their derived mixed oxides were all synthesized to be exploited as basic solid cata-

lysts. A commercially available catalyst 5 wt% Pt/Al<sub>2</sub>O<sub>3</sub> (Sigma Aldrich) was used in this work.

The LDH sample containing magnesium and aluminium was synthesized by the coprecipitation method. In this procedure, 100 mL of an aqueous solution of Mg(NO<sub>3</sub>)<sub>2</sub>·6H<sub>2</sub>O and Al(NO<sub>3</sub>)<sub>3</sub>·9H<sub>2</sub>O, with a Mg/Al molar ratio of 3, along with a solution of NaOH (1.0 mol L<sup>−1</sup>), as the precipitating agent, was added dropwise into a reactor containing 200 mL of ultrapure water at 70 °C and pH = 10, which was maintained constant during the whole synthesis. The obtained gel was aged at 70 °C for 12 h under nitrogen flow to minimize carbonate contamination. The resulting suspension was filtered and washed with ultrapure water to remove the excess of the precipitating agent. The solid was finally dried at 60 °C for 16 h.

A second sample was prepared by substituting nitrate anion NO<sub>3</sub><sup>−</sup>, and the eventual carbonate species CO<sub>3</sub><sup>2−</sup>, embedded between the lamellae of the previously synthesized LDH, for hydroxyl (OH<sup>−</sup>) groups. In this protocol, a part of the original material (LDH) was firstly turned into a mixed oxide by calcination at 800 °C for 4 h. The lamellar structure reconstruction was accomplished by adding the oxide solid into ultrapure water in a mass : volume ratio of 2 g : 15 mL. The suspension was stirred for 8 h and then filtered; the recovered solid was dried at 60 °C for 16 h.<sup>40</sup> This sample was named LDH-OH.

A third sample was prepared by exfoliating the initially precipitated LDH. In this procedure, the brucite-like layers were detached from each other providing single 2D nanosheets of Mg–Al double hydroxide. For preparing such a colloidal suspension, another part of the original LDH was dispersed in ultrapure water with the aid of an ultrasound for 10 min, maintaining a mass of the solid/volume ratio of 0.005. After this, the suspension was transferred to a Teflon-lined stainless steel autoclave and then subjected to hydrothermal treatment at 100 °C for 16 h.<sup>41</sup> This 2D sample was designated as nanoLDH.

Three more samples were prepared by calcining the original LDH under synthetic air flow (50 mL min<sup>−1</sup>) for 4 h. These 3D MgO–Al<sub>2</sub>O<sub>3</sub> mixed oxides were obtained at different calcination temperatures (500, 600 and 800 °C), leading to the formation of MgO–Al<sub>2</sub>O<sub>3</sub>-500, MgO–Al<sub>2</sub>O<sub>3</sub>-600 and MgO–Al<sub>2</sub>O<sub>3</sub>-800 samples, respectively.

### Solid characterization

X-ray diffraction analyses (XRD) were carried out in a Miniflex Rigaku diffractometer using CuK $\alpha$  radiation (1.5406 Å, 30 kV and 40 mA). The diffraction patterns were collected at a rate of 0.01° per step between 2° and 90°. The samples were analysed as powders without any pre-treatment.

LDH samples were analysed by thermogravimetry in TA Instruments SDT Q600. The samples were heated up to 1000 °C at a rate of 20 °C min<sup>−1</sup> under a synthetic air stream (30 mL min<sup>−1</sup>). The decomposition products were analysed in an Ametek Dymaxion quadrupolar mass spectrometer coupled on-line (TG-MS). Signals at *m/z* = 18, 30, 32, 44 and 46, related, respectively, to H<sub>2</sub>O<sup>+</sup>, NO<sup>+</sup>, O<sub>2</sub><sup>+</sup>, CO<sub>2</sub><sup>+</sup> and NO<sub>2</sub><sup>+</sup> were monitored.

The morphology of LDH and LDH-OH samples was examined by field emission scanning electron microscopy (FE-SEM) using a Quanta FEG 450 FEI microscope operating with an accelerating voltage of 20 kV. As for the 2D double hydroxide nanosheets, it was examined by transmission electron microscopy (TEM) using a FEI Tecnai microscope operating at 200 kV. Prior to examination, the nanoLDH sample was ultrasonically dispersed in isopropyl alcohol and then deposited on a copper grid coated with carbon film.

The chemical composition of the samples was determined by X-ray fluorescence spectrometry (XRF) in Bruker S8 Tiger equipment.

The porosity analysis was performed for the calcined LDH samples (MgO-Al<sub>2</sub>O<sub>3</sub> mixed oxides). The nitrogen adsorption and desorption isotherms were obtained at -196 °C in Micromeritics ASAP 2020 equipment. Specific surface areas were determined by BET formalism.

Temperature-programmed desorption of CO<sub>2</sub> (TPD-CO<sub>2</sub>) was used to characterize the surface basic sites of mixed oxide MgO-Al<sub>2</sub>O<sub>3</sub> samples. The solids were pretreated *in situ* under a flow of 8% O<sub>2</sub>/He (vol%) at 50 mL min<sup>-1</sup> in order to remove carbonate species engendered by air exposure. Different pretreatment temperatures were applied in accordance with the respective calcination temperature of each solid. Samples were then cooled down to room temperature and a flow of pure CO<sub>2</sub> was admitted into the reactor for 30 min. After purging the reactor, desorption was carried out by heating up the sample under He flow (50 mL min<sup>-1</sup>) following a rate of 20 °C min<sup>-1</sup> until the temperature at which the material was calcined.

### Catalytic tests

Catalytic chemoconversion of hydroxyacetone was performed in the liquid phase in a semi-batch glass reactor. The experiments were carried out at 40 °C, using a hydroxyacetone solution at 0.20 mol L<sup>-1</sup> as the starting material. Synthetic air was bubbled into the aqueous phase at 30 mL min<sup>-1</sup> throughout the experiment and the reaction medium was stirred at 1000 rpm to keep the contents perfectly mixed, favour gas diffusion and ensure kinetic control. Pt/Al<sub>2</sub>O<sub>3</sub> catalyst was previously reduced under hydrogen flow at 350 °C (10 °C min<sup>-1</sup>) for 1 h and then mixed with the basic solid at a 1:1 mass ratio. The reaction was monitored for a period of 6 h and aliquots were collected at every 30 min for the determination of hydroxyacetone conversion and product distribution.

The concentration of the reaction products was determined by high performance liquid chromatography (HPLC) in Waters Alliance e2695 equipped with a refractive index detector (RID) and a photodiode array detector (PDA). A Biorad Aminex HPX-87H column was used at 65 °C in isocratic elution mode with a 5 mmol L<sup>-1</sup> H<sub>2</sub>SO<sub>4</sub> solution as the mobile phase at a flow of 0.7 mL min<sup>-1</sup>. The temperature of RID was kept constant at 50 °C and the analyses at PDA were performed at 210 nm.

The results of the reaction runs were analyzed in terms of hydroxyacetone conversion and selectivity

$$S_p = \text{selectivity to product } p = 100 \times \frac{n_C C_p}{\sum n_C C_p}$$

The  $n_C$  are the number of carbon atoms in the products of hydroxyacetone chemoconversion and  $C_p$  are the concentrations of the main identifiable compounds, namely lactic acid, pyruvic acid and pyruvaldehyde.

The catalyst reusability was evaluated by performing two consecutive reaction runs of 6 h each. Right after the first run, the catalyst was filtered, dried overnight, calcined at 500 °C and finally reduced under hydrogen flow at 350 °C (10 °C min<sup>-1</sup>) for 1 h. The second catalytic run was then carried out following exactly the same protocol described before.

## Results and discussion

A detailed discussion on the main physico-chemical characteristics of the commercial Pt/Al<sub>2</sub>O<sub>3</sub> catalyst can be found elsewhere.<sup>39</sup> This commercial sample essentially presents platinum nanoparticles (4.6 nm) highly dispersed on a high surface area transition  $\gamma$ -Al<sub>2</sub>O<sub>3</sub>.<sup>39</sup>

The as-synthesized LDH basic catalysts were initially analysed by XRD in order to guarantee the formation of a layered structure. Fig. 1 shows the diffractograms obtained for LDH and LDH-OH samples and they both exhibit diffraction patterns typical of the aimed lamellar hydrotalcite-type structure (JCPDS no. 22-700). This finding revealed that the lamellar structure destroyed upon calcination to release the nitrate/carbonate anions was indeed reconstructed into LDH-OH after rehydration. Such structural restoration is indeed well-known

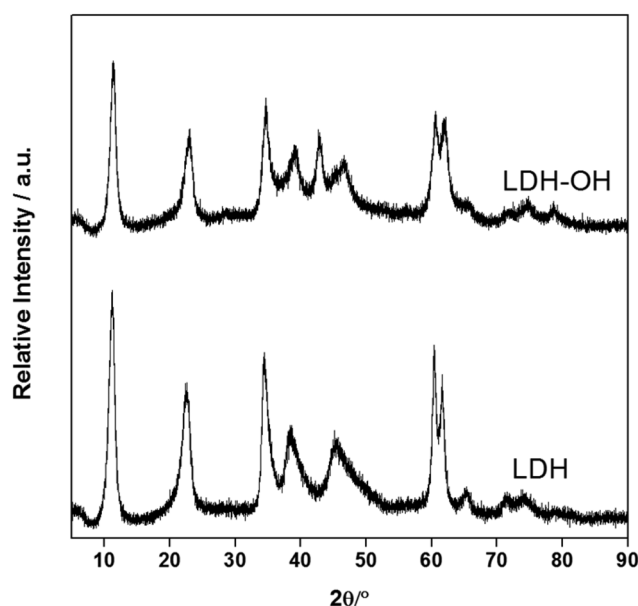


Fig. 1 Diffraction patterns of synthesized LDH samples.

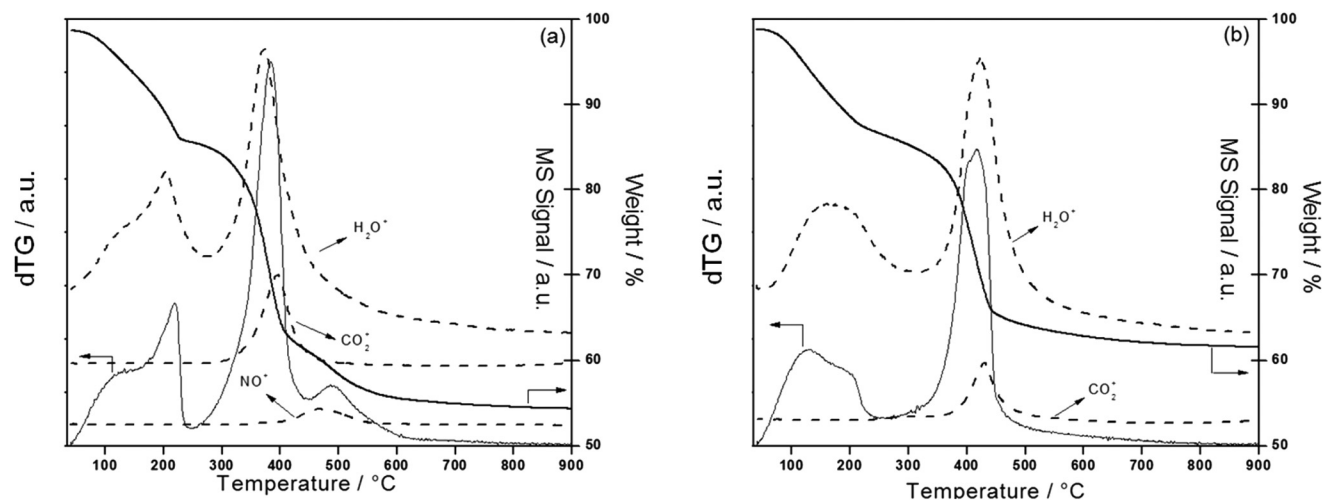


Fig. 2 TG-MS profiles of (a) LDH and (b) LDH-OH samples.

in the literature<sup>40,42</sup> and it is a consequence of the memory effect of hydrotalcite-like materials.<sup>42</sup> Nonetheless a new diffraction at 42.84° can be seen in the reconstructed LDH-OH sample, which can be ascribed to a reminiscent magnesium oxide cubic structure (JCPDS no. 45-0946) formed before rehydration.

The interlayer spaces were estimated from the (003) plane at an ~11° Bragg angle and it was found to decrease from 0.794 nm (LDH) to 0.772 nm (LDH-OH). It matches indeed the expected shortening promoted by replacing larger NO<sub>3</sub><sup>−</sup> to OH<sup>−</sup> anions in the interlamellar domain as it is well-known that such a space is determined by the dimensions of the ion species embedded in between.<sup>42</sup> It should be mentioned though that the LDH interlayer spacing as assessed by XRD falls in an intermediate value if one considers the sole occurrence of either NO<sub>3</sub><sup>−</sup> (0.879 nm) or CO<sub>3</sub><sup>2−</sup> (0.765 nm).<sup>42</sup> Similarly, the value for LDH-OH is higher than the theoretical one (0.755 nm).<sup>42</sup> These trends suggest that some CO<sub>2</sub> was also able to find its way into the interlamellar domain during coprecipitation and reconstruction procedures despite the nitrogen flushing. This discussion was indeed corroborated by identifying the products released during thermal decomposition in TG-MS analyses (Fig. 2).

Some differences can be seen in the thermograms; while four thermal events are registered for LDH, decomposition of LDH-OH occurs in three stages. The thermal events occurring below 240 °C are associated with the elimination of water (adsorbed and that present between the lamellae of the materials) and the mass loss in intermediate temperatures (240–445 °C) is related to the dehydroxylation of the hydrotalcite-type structure along with the release of interlamellar carbonate species as identified by the CO<sub>2</sub> (*m/z* = 44) profile registered in the mass spectrometer. A fourth event at high temperature (>450 °C) is only seen by the LDH sample and corresponds to the removal of NO<sub>3</sub><sup>−</sup> species from the interlayer space. These data are quite consistent with those reported else-

where<sup>42,43</sup> and the absence of such a thermal event in LDH-OH thermogram confirms the replacement of the compensating nitrate anions during the lamellar material reconstruction process.

In order to verify the morphology of the lamellar samples and observe the occurrence of eventual morphological changes from LDH to LDH-OH, both samples were examined by FE-SEM and representative images are displayed in Fig. 3. It can be seen that they exhibit similar morphological characteristics, being formed by aggregates of plentiful thin plates as typically observed for lamellar materials.<sup>44,45</sup>

The nanoLDH sample was characterized only by TEM to ensure the efficient formation of double hydroxide nanosheets. One should bear in mind that this material can only be obtained as a 2D nanostructure in a colloidal suspension, since the original nanosheet stacking immediately occurs by removing the solvent and restoring the layered structure.<sup>46</sup> A representative TEM image of the exfoliated LDH is also depicted in Fig. 3, revealing that the isolated lamellae are indeed irregular hexagonal nanoplates with a wide size distribution ranging from 30 to 100 nm.

The three activated LDH samples (calcined solids) were analysed regarding their crystalline structure, porosity and surface basicity. As expected, their diffractograms show that the lamellar structure is completely destroyed after calcination at temperatures as low as 500 °C. As a matter of fact, the diffractograms are quite similar regardless of the calcination temperature (Fig. 4), exhibiting peaks related to the cubic structure of the MgO periclase phase (space group *Fm3m*). The lattice parameters collected in Table 1 are consistent with a bare MgO structure, indicating that a segregated alumina phase is obtained upon calcination. However, no other crystalline phase was identified in the XRD patterns, which suggests that an amorphous or low-crystalline alumina is formed. Finally, MgO mean particle size is seen to increase gradually by raising the calcination temperature (Table 1).



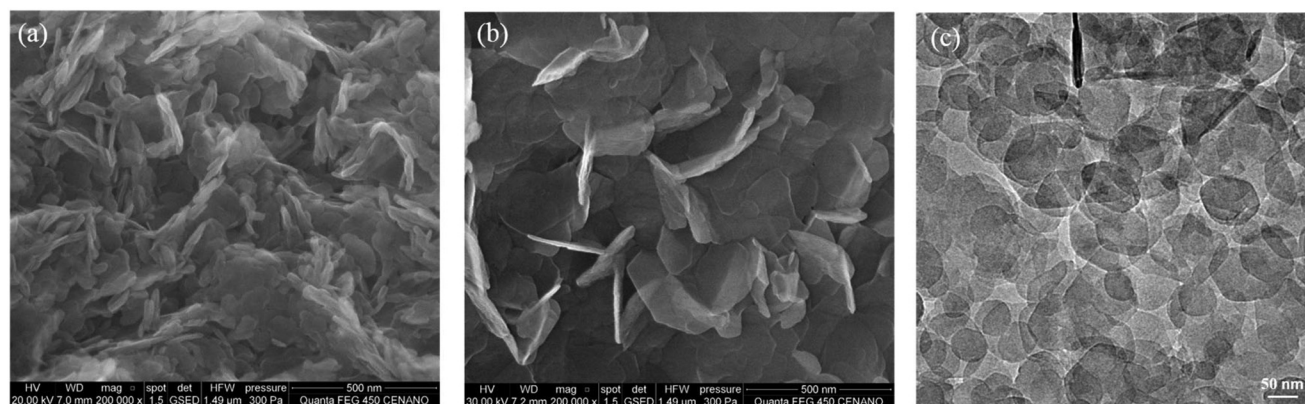


Fig. 3 Representative SEM images of (a) LDH and (b) LDH-OH samples and a TEM image of (c) nanoLDH sample.

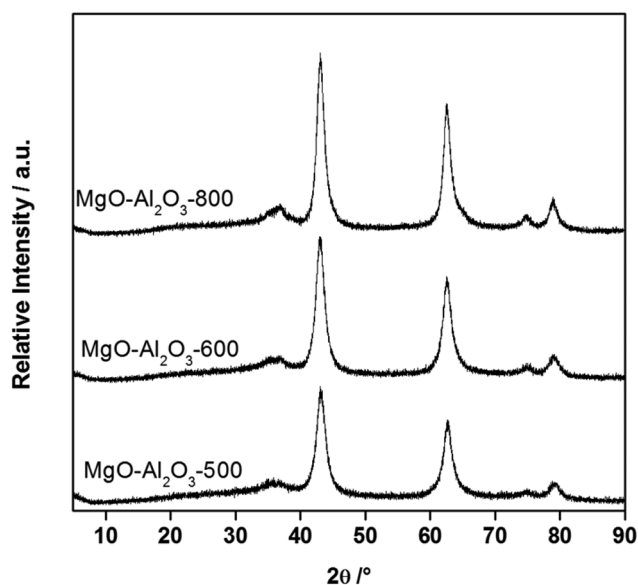


Fig. 4 Diffraction pattern of MgO–Al<sub>2</sub>O<sub>3</sub> mixed oxides.

BET surface areas are also summarized in Table 1. All materials present high surface areas as expected for mixed oxides obtained from layered double hydroxide precursors. An important increase ( $\sim 40\%$ ) in surface area is seen when calcination temperature is raised from 500 to 600 °C and then a

slight decrease is detected by further increasing the temperature to 800 °C. Such a trend can be rationalized by the thermal decomposition dynamics of LDH as previously discussed herein. As the total decomposition of the double hydroxide precursor only occurs at above 600 °C (Fig. 2), the development of a porous structure, and as a consequence higher surface area, can be expected from samples MgO–Al<sub>2</sub>O<sub>3</sub>-500 to MgO–Al<sub>2</sub>O<sub>3</sub>-600; once it is generated, the onset of porous structure collapse or sintering may occur, gradually leading to a drop in surface area (MgO–Al<sub>2</sub>O<sub>3</sub>-800).

Temperature-programmed desorption of CO<sub>2</sub> was used to qualitatively and quantitatively estimate the distribution of surface basic sites of the calcined materials; the profiles are depicted in Fig. 5 and the total density of basic sites is listed in Table 1. All samples present similar patterns, a desorption peak at low temperatures ( $<200$  °C) and a long tail extending to higher temperatures, evidencing a wide distribution of distinct basic sites. The experimental curves were thus mathematically decomposed considering multiple Gaussian contributions. The position of each peak was determined from an initial estimative and the calculations were conducted based on a nonlinear routine to minimize the deviations of the squares.<sup>47</sup> The desorption temperature is intimately associated with the basic site strength; the higher the desorption temperature, the stronger the basic sites. Thus, the basic sites were divided into weak (up to 170 °C), medium (between 170 and 270 °C) and strong (above 270 °C). Though empirical, these

**Table 1** Lattice parameter ( $a$ ), MgO mean particle size ( $d_{\text{MgO}}$ ), BET surface area ( $S_{\text{BET}}$ ) and density of weak, medium and strong basic sites of MgO–Al<sub>2</sub>O<sub>3</sub> samples

Basic catalyst	$a$ (nm)	$d_{\text{MgO}}$ (nm)	$S_{\text{BET}}$ (m <sup>2</sup> g <sup>−1</sup> )	Basic sites				
				Weak (%)	Medium (%)	Strong (%)	Total (mmol m <sup>−2</sup> )	Total (mmol g <sup>−1</sup> )
MgO–Al <sub>2</sub> O <sub>3</sub> -500	0.419	5.51	187	42	23	35	544	101
MgO–Al <sub>2</sub> O <sub>3</sub> -600	0.420	5.75	256	40	27	33	187	45
MgO–Al <sub>2</sub> O <sub>3</sub> -800	0.420	6.53	225	78	15	7	85	18

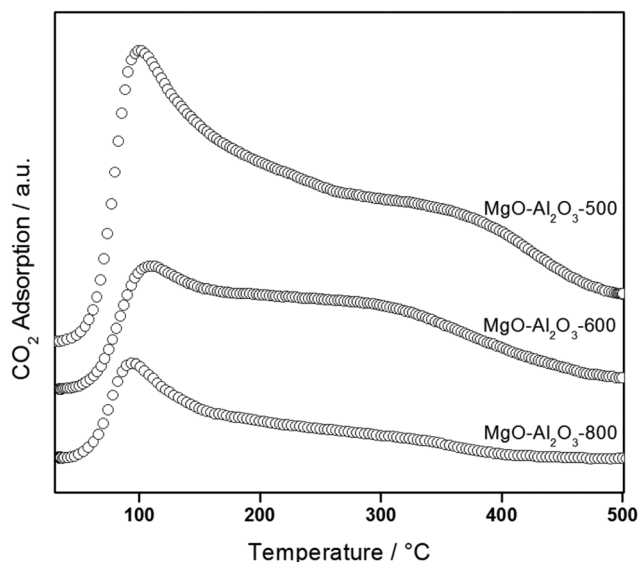


Fig. 5 TPD- $\text{CO}_2$  profiles of  $\text{MgO}-\text{Al}_2\text{O}_3$  mixed oxides.

temperature ranges are commonly used in the literature and are very useful as a rough guide to assign basic strength and compare and contrast surface site distribution.

Despite exhibiting similar desorption profiles, the density of each basic site is different. The solid activated at 500 °C has the highest density of sites roughly equally distributed among the three types. The increase of the calcination temperature caused a very sharp decrease in the total concentration of basic sites but kept a similar strength distribution. At the highest calcination temperatures, the density drops even further and the presence of weak base sites is dominant (~80%).

All base solids were evaluated in the aqueous-phase conversion of hydroxyacetone to lactic acid as a part of a dual metal/base heterogeneous catalytic system. In order to obtain such a system, base solids were mixed with a previously reduced  $\text{Pt}/\text{Al}_2\text{O}_3$  commercial catalyst in a 1 : 1 mass ratio. Catalytic con-

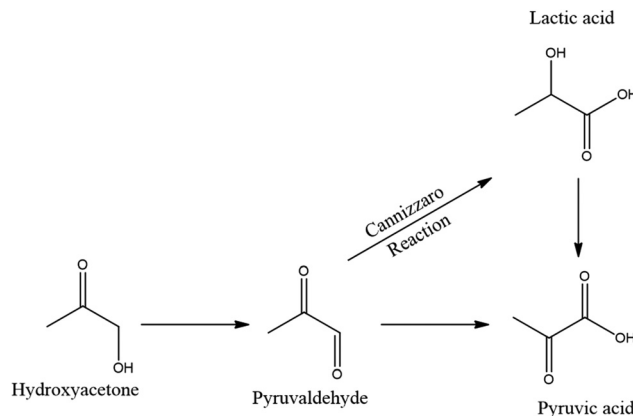


Fig. 6 Reaction scheme for the catalytic transformation of hydroxyacetone into lactic acid.

version of hydroxyacetone under an oxidative atmosphere may lead to a wide variety of organic compounds and even carbon dioxide if completely oxidized. Fig. 6 depicts a simplified reaction scheme highlighting only the more relevant C3 chemicals.

Hydroxyacetone oxidation/oxidative dehydrogenation of the metal catalyst would lead to pyruvaldehyde, which may be further oxidised to pyruvic acid. The intramolecular disproportionation (Cannizzaro reaction) of the intermediate pyruvaldehyde to lactic acid on the base catalyst also has to be taken into consideration. It has indeed been reported that such rearrangement easily occurs in alkaline medium.<sup>19,33,39</sup> Finally, the undesired oxidation of lactic acid to pyruvic acid is also possible.

Initially, some control experiments were performed in order to examine the role played by each component of the dual metal/base catalytic system. It is firstly worth mentioning that no conversion of hydroxyacetone occurs without either catalyst. By using only the  $\text{Pt}/\text{Al}_2\text{O}_3$  metal catalyst (Table 2, entry 1), pyruvic acid and pyruvaldehyde are the major products and only around 5% of hydroxyacetone is converted within 6 h.

**Table 2** Initial rate ( $r_0$ ), selectivity to lactic acid ( $S_{\text{LA}}$ ), pyruvic acid ( $S_{\text{PA}}$ ) and pyruvaldehyde ( $S_{\text{PAL}}$ ) on basic catalysts derived from lamellar double hydroxides

Entry	Catalytic system	$r_0^a$ ( $\text{mol g}^{-1} \text{h}^{-1}$ )	$X^b$ (%)	$S_{\text{LA}}^c$ (%)	$S_{\text{PA}}^c$ (%)	$S_{\text{PAL}}^c$ (%)	$\text{pH}^d$
1	$\text{Pt}/\text{Al}_2\text{O}_3$	0.9	4.7	20	33	47	4.7
2	$\text{MgO}-\text{Al}_2\text{O}_3^e$	0.5	11.1	100	—	—	8.3
3	$\text{Pt}/\text{Al}_2\text{O}_3 + \text{LDH}$	1.6	20.1	32	63	6	5.6
4	$\text{Pt}/\text{Al}_2\text{O}_3 + \text{LDH-OH}$	1.8	19.9	21	74	5	5.7
5	$\text{Pt}/\text{Al}_2\text{O}_3 + \text{nanoLDH}$	1.2	20.1	20	54	27	5.9
6	$\text{Pt}/\text{Al}_2\text{O}_3 + \text{MgO}-\text{Al}_2\text{O}_3\text{-500}$	4.7	21.0	51	49	—	9.5
7	$\text{Pt}/\text{Al}_2\text{O}_3 + \text{MgO}-\text{Al}_2\text{O}_3\text{-600}$	3.1	23.1	63	37	—	9.4
8	$\text{Pt}/\text{Al}_2\text{O}_3 + \text{MgO}-\text{Al}_2\text{O}_3\text{-800}$	3.5	21.2	66	34	—	9.2
9	$\text{Pt}/\text{MgO}-\text{Al}_2\text{O}_3\text{-800}$	3.5	20.7	100	—	—	10.5

<sup>a</sup> Reaction rate as normalized by metal catalyst weight only. <sup>b</sup> Conversion of hydroxyacetone under isoconversion conditions. <sup>c</sup> Selectivity at isoconversion of ~20%. <sup>d</sup> pH of reaction medium (hydroxyacetone + catalysts) at the beginning of the reaction. <sup>e</sup> Reaction rate as normalized by base catalyst weight only.

On the other hand, lactic acid is the only product detected when  $\text{MgO-Al}_2\text{O}_3$  mixed oxide base catalyst is used instead (Table 2, entry 2). It suggests that the acid is formed from hydroxyacetone dehydrogenation to pyruvaldehyde, which is rearranged to lactic acid, all steps occurring on the base surface sites. The LDH catalyst, however, showed no activity at all, which is probably related to its lower basicity when compared to the mixed oxides. All in all, these control experiments show that neither the metal catalyst nor the base solids alone are kinetically and/or selectively effective for hydroxyacetone chemoconversion to lactic acid. At the same time, they outline the key role played by the base centres on selectivity.

As for the dual catalytic systems, it can be easily noticed that they are definitely more active than the sole metal or base catalysts (Table 2). However they behave quite differently and can indeed be divided in two sets; the less active systems, leading preferentially to the formation of pyruvic acid, are formed by the ones containing double hydroxides as base catalysts (Table 2, entries 3–5), while those comprising mixed oxides are significantly more active and selective to lactic acid (Table 2, entries 6–8).

Irrespective of the anion embedded within the LDH interlamellar domain (nitrate, entry 3 or hydroxyl, entry 4 in Table 2) or the double hydroxide topology (lamellar, entry 3 or exfoliated 2D nanosheets, entry 5 in Table 2) the reaction rates are higher than those estimated for the bare metal catalyst (Table 2, entry 1). Lactic acid is formed with selectivities around 20–30% and pyruvaldehyde is also detected; however, product distribution is defined by the selective formation of pyruvic acid (55–75%). Despite the similar behaviour at first sight, the time-resolved selectivity profiles displayed in Fig. 7 reveal that these double hydroxide-based dual systems exhibit significantly different reaction dynamics according to the topology of the base solids.

On the systems composed of lamellar structured base catalysts (LDH and LDH-OH), lactic acid is initially formed along with pyruvic acid and pyruvaldehyde (Fig. 7a and b). It indicates that oxidative dehydrogenation of hydroxyacetone to pyruvaldehyde on the metal catalyst and its subsequent disproportionation on the base solid take place. The presence

of a base catalyst may also catalyse the interconversion of hydroxyacetone to lactaldehyde; this prototropic tautomer may be oxidised on metal sites to lactic acid. This tautomerization route as a first reaction step cannot be ruled out. The formation of pyruvic acid, however, increases steadily over time and the selectivity trends allow the conclusion that it may be formed from lactic acid oxidation.

As for the dual system using nanoLDH colloidal suspension as a heterogeneous catalyst (Fig. 7c), a contrasting selectivity to pyruvaldehyde can be observed. Such striking high selectivity (Table 2, entry 5) indicates the limited activity of 2D double hydroxide nanosheets in the base-induced intramolecular disproportionation of pyruvaldehyde to lactic acid. This fashion might also be associated with the presence of acidic nitrate anions that are set free in the reaction medium upon exfoliation of the original double hydroxide lamellar structure. It is interesting to notice, however, that the selectivity to lactic acid is roughly the same within the whole reaction period while an interdependence between pyruvaldehyde and pyruvic acid is clearly established in the selectivity profiles displayed in Fig. 7c. This result suggests that the formation of lactic acid on this  $\text{Pt/Al}_2\text{O}_3$  + nanoLDH dual system might not involve the Cannizzaro reaction as previously observed for the lamellar systems but proceeds only *via* tautomerization of hydroxyacetone followed by the tautomer oxidation instead.

These findings allow the proposition that simultaneous conversion of hydroxyacetone *via* parallel reactions can take place over LDH-containing dual catalytic systems but following distinct routes according to the base catalyst topology. A general schematic reaction pathway considering the lamellar and 2D nanosheet structures for the base solid is presented in Fig. 8a and b, respectively.

The second set of dual catalytic systems is constituted of mixed oxides as the base solid component (Table 2, entries 6–8). These systems are meaningfully more active, presenting reaction rates approximately 4–5 times higher than those valued for the sole  $\text{Pt/Al}_2\text{O}_3$  catalyst (Table 2, entry 1). Lactic acid is always the primary product with selectivities above 50%, notably higher than those reached with the previous catalytic systems reported herein. Unlike the double hydroxide-

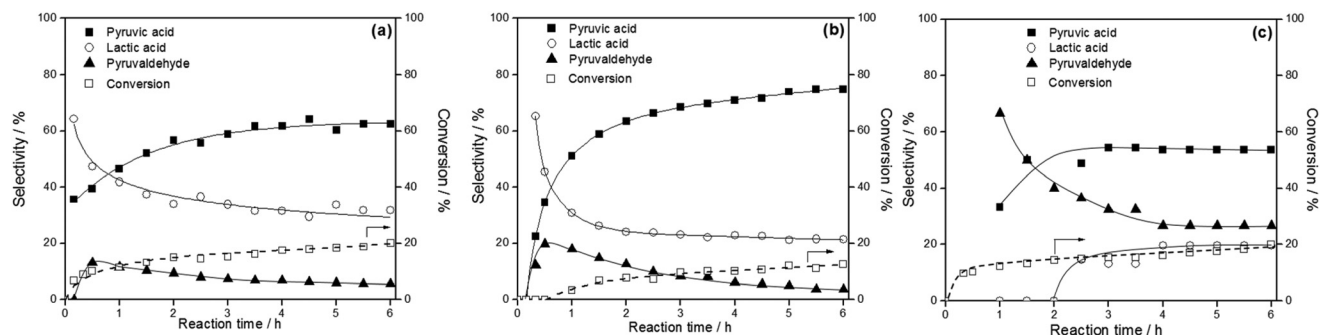


Fig. 7 Time-resolved selectivity curves and hydroxyacetone conversion over dual catalytic systems comprised of a 1 : 1 mass ratio of metal catalyst and double layered hydroxides: (a)  $\text{Pt/Al}_2\text{O}_3$  + LDH, (b)  $\text{Pt/Al}_2\text{O}_3$  + LDH-OH and (c)  $\text{Pt/Al}_2\text{O}_3$  + nanoLDH.

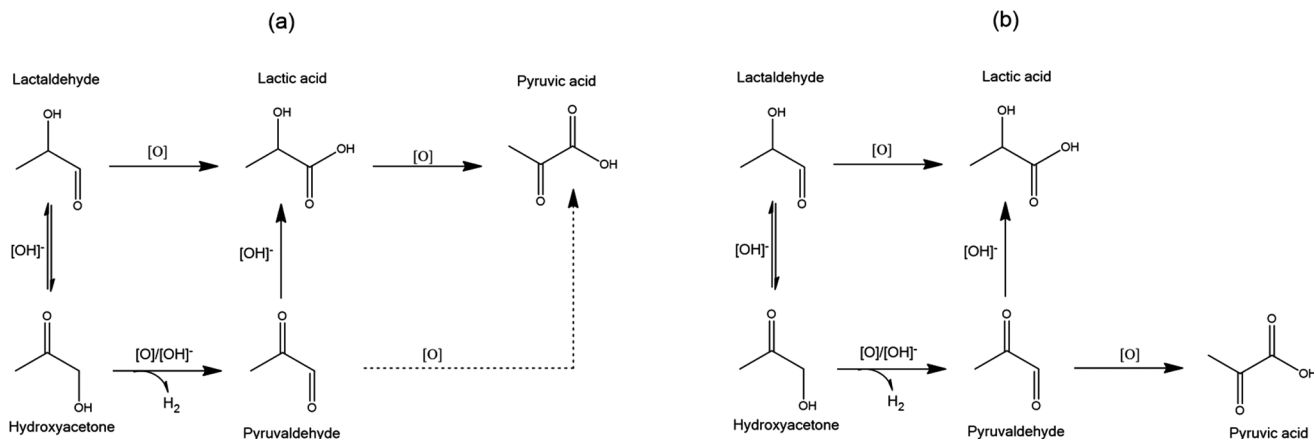


Fig. 8 Schematic reaction pathway for the conversion of hydroxyacetone over dual catalytic systems containing double hydroxides with (a) lamellar and (b) 2D exfoliated nanosheet structures as base heterogeneous catalysts.

containing systems, pyruvic acid is the only other product formed and no traces of pyruvaldehyde were detected whatsoever. Therefore hydroxyacetone tautomerization and the subsequent oxidation could be thought at first as the key reaction route for lactic acid production. This different behaviour can be associated with the different basicity of the solid base catalysts as already mentioned. The more basic medium provided by using the  $\text{MgO-Al}_2\text{O}_3$  mixed oxides is evident by the higher pH value of the reaction aqueous phase as summarized in Table 2. Nevertheless, complementary experiments carried out with pyruvaldehyde as the initial substrate instead of hydroxyacetone showed that the aldehyde is promptly converted to lactic acid through Cannizzaro reaction. Similar findings have indeed been reported elsewhere.<sup>19,33,39</sup> These outcomes lead us also to consider the intermediate formation of pyruvaldehyde and its immediate base-induced disproportionation to lactic acid.

Time-resolved trends for the distribution of products (Fig. 9) indicate that these 3D oxide-containing dual systems behave likewise and the cascade oxidation of lactic acid to pyruvic acid is also seen to proceed on these systems. Nonetheless, this chemoconversion interdependence is kinetically

shifted to longer times (or higher hydroxyacetone conversion) correlating well with the estimated reaction rates as normalized by metal catalyst weight (Table 2), suggesting that the more active the catalytic systems the faster the further oxidation of lactic to pyruvic acid. Such a trend is in close agreement with the results reported elsewhere on the use of a homogeneous alkaline catalyst.<sup>39</sup>

Lastly, the time-resolved curves allow better differentiation of the performance of these dual systems and tuning the operation conditions in order to optimize lactic acid yields. Despite the over oxidation of lactic acid upon reaction time, the outstanding behaviour of  $\text{Pt/Al}_2\text{O}_3 + \text{MgO-Al}_2\text{O}_3\text{-800}$  easily comes out as 100% selectivity toward lactic acid can be accomplished along the first hour. It brings up the possibility of settling a highly selective process by adjusting reaction time and developing a more suitable process set up with series reactors and/or continuous recirculation of the liquid feed.

All results presented herein reveal that the production of lactic acid from hydroxyacetone proceeds *via* cascade reactions and that a multitude of different combinations may lead to lactic acid formation. Since the dual systems investigated in this work comprise two separate solid catalysts, *i.e.* the metal

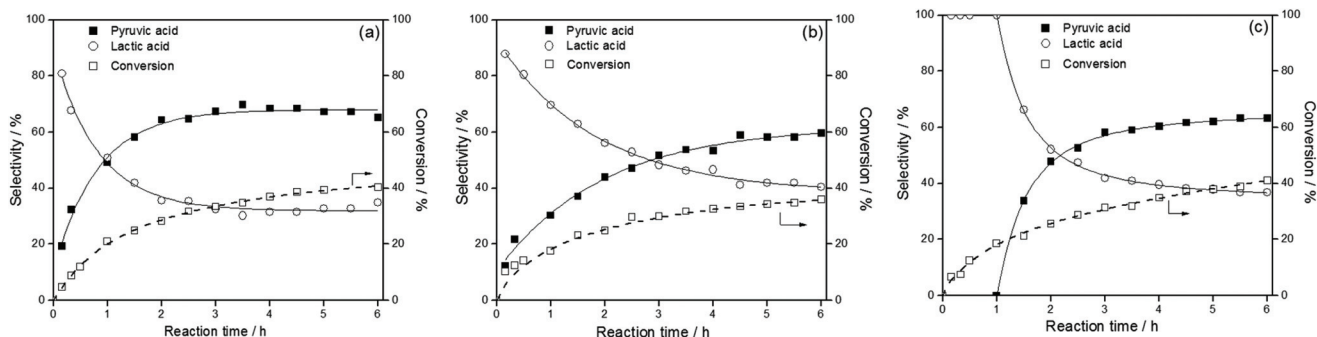


Fig. 9 Time-resolved selectivity curves and hydroxyacetone conversion over dual catalytic systems comprised of a 1 : 1 mass ratio of metal catalyst and mixed oxides: (a)  $\text{Pt/Al}_2\text{O}_3 + \text{MgO-Al}_2\text{O}_3\text{-500}$ , (b)  $\text{Pt/Al}_2\text{O}_3 + \text{MgO-Al}_2\text{O}_3\text{-600}$  and (c)  $\text{Pt/Al}_2\text{O}_3 + \text{MgO-Al}_2\text{O}_3\text{-800}$ .



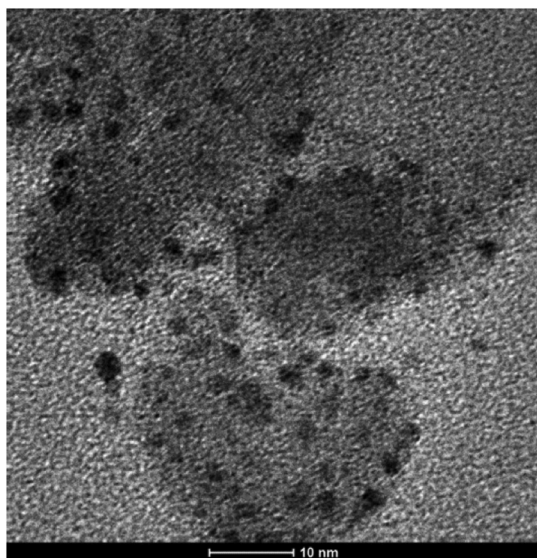


Fig. 10 Representative TEM image of the Pt/MgO–Al<sub>2</sub>O<sub>3</sub>-800 bifunctional catalyst.

and base surface sites are set utterly apart from each other, it is conceivable that the reaction pathway would depend on each of those two catalysts the hydroxyacetone molecule would first meet in the reaction medium and adsorb on. Likewise it is also reasonable that once the lactic acid formed from any cascade combination desorbs from the catalyst surface and diffuses into the liquid phase it can be oxidized to pyruvic acid on the metal catalyst since they are both kept in the same reactor. A different arrangement of the surface active sites could thus disturb this reaction network dynamics and bring some benefit to the chemoselective formation of the desired acid, driving the design of a more robust solid catalyst and/or a more cost-effective catalytic process.

Therefore, to assess the relevance of such surface site disposals, a bifunctional catalyst was synthesized taking the MgO–Al<sub>2</sub>O<sub>3</sub>-800 as a basic support for platinum metal nanoparticles (Pt/MgO–Al<sub>2</sub>O<sub>3</sub>-800). This catalyst was characterized as concerning chemical composition and metal dispersion by X-ray fluorescence spectrometry and transmission electron microscopy, respectively. It was seen that it presented practically the same platinum content (4.7 wt%) as the Pt/Al<sub>2</sub>O<sub>3</sub> used in the dual systems but with much smaller metal nanoparticles (2.4 nm). A representative TEM image is depicted in Fig. 10.

The reaction rate obtained for this sample (Table 2, entry 9) disclosed that it is as active as its parent dual system (Table 2, entry 8). Nevertheless, this bifunctional catalyst revealed to be remarkably selective to lactic acid (99%) with only small amounts of a side product (pyruvic acid) within the whole period of the reaction, as presented in Fig. 11. This notable performance is likely related to the active site assemblies, which are now set together on the same surface (vicinal sites). Such vicinity may facilitate the one-step conversion of hydroxyacetone to lactic acid; that is to say that after the adsorption

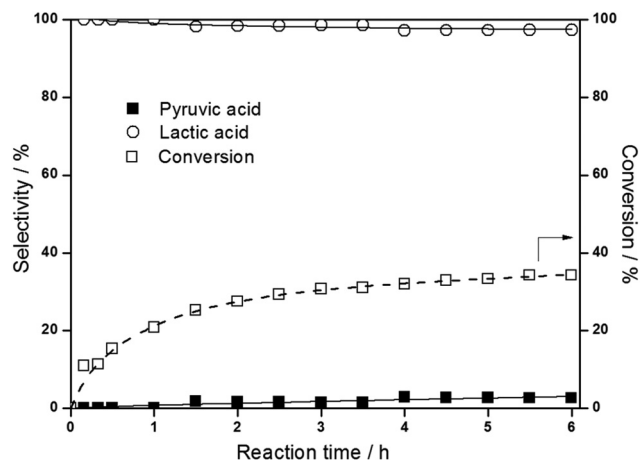


Fig. 11 Time-resolved selectivity curves and hydroxyacetone conversion over Pt/MgO–Al<sub>2</sub>O<sub>3</sub>-800 bifunctional catalyst.

of the hydroxyacetone molecule, the intermediate pyruvaldehyde formed through oxidative dehydrogenation on a metal centre is immediately rearranged to lactic acid on the vicinal basic site before leaving the catalyst surface. The subsequent oxidation of the desorbed lactic acid is likely avoided due to the preferential adsorption of hydroxyacetone on metal sites. It is definitely a noteworthy result for a heterogeneous catalyst since such chemoselectivity is usually reached over biochemical systems.

Due to the expressive result, the spent bifunctional catalyst was recovered by filtration right after reaction, dried and characterized as regarding its crystalline structure. Its XRD pattern is compared and contrasted with that obtained from the fresh sample in Fig. 12.

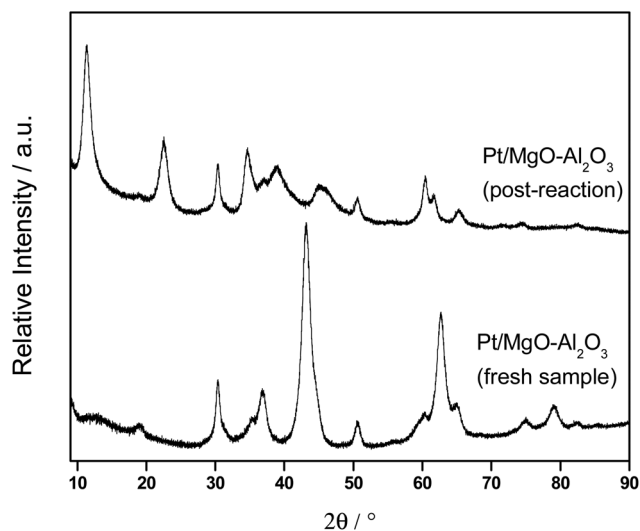


Fig. 12 Diffraction pattern of Pt/MgO–Al<sub>2</sub>O<sub>3</sub>-800 bifunctional catalyst before (fresh sample) and after (post-reaction) aqueous-phase reaction.

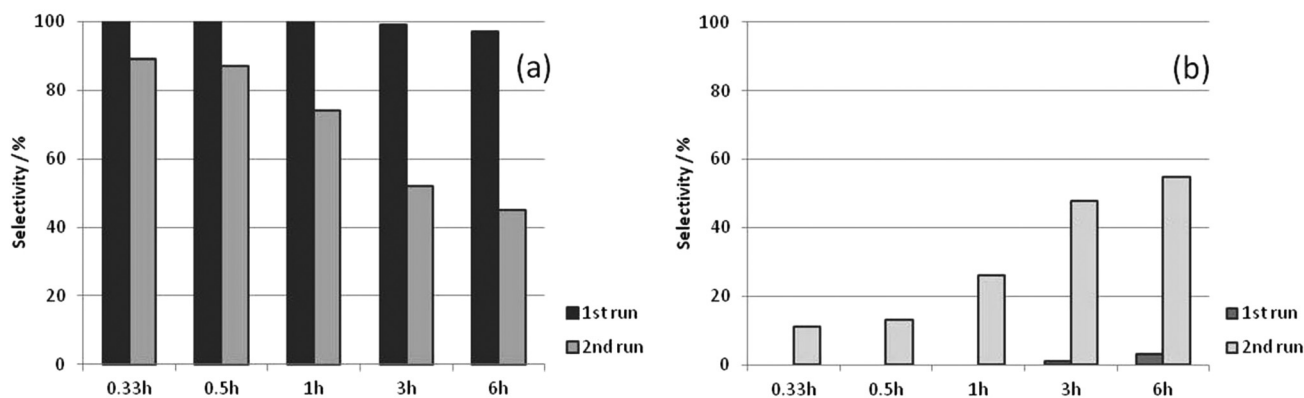


Fig. 13 Selectivity to lactic acid (a) and pyruvic acid (b) for two consecutive reaction runs over Pt/MgO–Al<sub>2</sub>O<sub>3</sub>–800 bifunctional catalyst.

It is seen that the mixed oxide 3D structure modifies upon hydroxyacetone aqueous-phase processing as new diffraction peaks were detected after reaction. As a matter of fact, the XRD analysis revealed that the catalyst turns back into a lamellar structure, which is quite clear for the rising diffraction peaks at 11.4° and 22.5°. This behaviour can indeed be expected due to the well-known memory effect of such solids as discussed hereinbefore, which favours the oxide rehydration to a double hydroxide and the consequent regeneration of the layered topology.

To evaluate the bifunctional catalyst reusability, the dried spent catalyst was firstly calcined in order to reconstruct the 3D structure of the original mixed oxide-supported sample. This reassembling is rather important to perform a second reaction cycle ensuring that it starts with the same catalyst, *i.e.* with a sample with the same chemical and structural features.

The catalyst revealed to be as active as in the first run as disclosed by the reaction rate (3.7 mol g<sup>-1</sup> h<sup>-1</sup> in the second run *versus* 3.5 mol g<sup>-1</sup> h<sup>-1</sup> in the first run). Accordingly, the selectivity to lactic acid was also high (90%) at the beginning of the reaction with only a minor formation of pyruvic acid. However, contrarily to what was seen in the first run, lactic acid selectivity dropped gradually with time (Fig. 13a) along with an ever-increasing selectivity to pyruvic acid (Fig. 13b). This fashion indicates some change in the distribution of surface sites during recycling which must be taken into consideration to further optimize the design of a bifunctional heterogeneous catalyst bearing metal and base centres.

The results reported herein prove the feasibility of the establishment of a promising green process that would meet the technological challenges of catalyst separation and corrosiveness while keeping biochemical-like high selectivity to lactic acid.

## Conclusions

The results presented herein show that it is possible to selectively produce lactic acid from the aqueous-phase conversion

of hydroxyacetone over a heterogeneous catalyst dual system. For a single Pt metal catalyst, activity and chemoselectivity of the dual system can be tuned by the morphology, topology and basicity of the base catalyst. Catalytic activity was up to five times higher by adding a heterogeneous base solid to the metal catalyst. Lactic acid selectivity was raised from 20–30% to 50–70% by changing from lamellar double hydroxide to 3D mixed oxide base catalysts. Surface site distribution was also shown to be quite decisive for the catalyst performance; the proximity of metal and basic centres on the same surface rendered a highly selective bifunctional catalyst. A remarkable 100% selectivity to lactic acid was reached and the undesired cascade oxidation of lactic to pyruvic acid was hindered.

## Acknowledgements

The authors acknowledge the financial support from CNPq and FAPERJ. Mr Francisco Rangel (INT) is also thanked for his valuable assistance with the FE-SEM analyses. Ms Nataly Amorim (CETENE) and Dr A.M. Duarte de Farias (INT) are also acknowledged for their support with TEM examination. E. M. A. also thanks CAPES for the scholarship.

## References

- 1 J. Chaminand, L. Djakivitch, P. Gallezot, P. Marion, C. Pinel and C. Rosier, *Green Chem.*, 2004, **6**, 359–361.
- 2 M. A. Dasari, P.-P. Kiatsimkul, W. R. Sutterlin and G. J. Suppes, *Appl. Catal., A*, 2005, **281**, 225–231.
- 3 T. Miyazawa, S. Koso, K. Kunimori and K. Tomishige, *Appl. Catal., A*, 2007, **318**, 244–251.
- 4 K. Klepáčová, D. Mravec and M. Bajus, *Appl. Catal., A*, 2005, **294**, 141–147.
- 5 R. S. Karinen and A. O. I. Krause, *Appl. Catal., A*, 2006, **306**, 128–133.
- 6 N. Dimitratos, F. Porta and L. Prati, *Appl. Catal., A*, 2005, **291**, 210–214.

- 7 N. Dimitratos, F. Porta, L. Prati and A. Villa, *Catal. Lett.*, 2005, **99**, 181–185.
- 8 C. L. Bianchi, P. Canton, N. Dimitratos, F. Porta and L. Prati, *Catal. Today*, 2005, **102–103**, 203–212.
- 9 S. Demirel, K. Lehnert, M. Lucas and P. Claus, *Appl. Catal., B*, 2007, **70**, 637–643.
- 10 H. Kishida, F. Jin, Z. Zhou, T. Moriya and H. Enomoto, *Chem. Lett.*, 2005, **34**, 1560–1561.
- 11 Z. Shen, F. Jin, Y. Zhang, B. Wu, A. Kishita, K. Tohji and H. Kishida, *Ind. Eng. Chem. Res.*, 2009, **48**, 8920–8925.
- 12 W. Amass, A. Amass and B. Tighe, *Polym. Int.*, 1998, **47**, 89–144.
- 13 M. Jamshidian, E. A. Tehrany, M. Imran, M. Jacquot and S. Desobry, *Compr. Rev. Food Sci. Saf.*, 2010, **9**, 552–571.
- 14 K. Hofvendahl and B. Hahn-Hägerdal, *Enzyme Microb. Technol.*, 2000, **26**, 87–107.
- 15 S.-Q. Liu, *Int. J. Food Microbiol.*, 2003, **83**, 115–131.
- 16 R. P. John, G. S. Anisha, K. M. Nampoothiri and A. Pandey, *Biotechnol. Adv.*, 2009, **27**, 145–152.
- 17 R. P. John, K. M. Nampoothiri and A. Pandey, *Appl. Microbiol. Biotechnol.*, 2007, **74**, 525–534.
- 18 T. Tsujino, S. Ohigashi, S. Sugiyama, K. Kawashiro and H. Hayashi, *J. Mol. Catal.*, 1992, **71**, 25–35.
- 19 N. Dimitratos, J. A. Lopez-Sanchez, S. Meenakshisundaram, J. M. Anthonykutti, G. Brett, S. H. Taylor, D. W. Knight and G. J. Hutchings, *Green Chem.*, 2009, **11**, 1209–1216.
- 20 R. Datta, S.-P. Tsai, P. Bonsignore, S.-H. Moon and J. R. Frank, *FEMS Microbiol. Rev.*, 1995, **16**, 221–231.
- 21 R. Datta and M. Henry, *J. Chem. Technol. Biotechnol.*, 2006, **81**, 1119–1129.
- 22 M. Bicker, S. Endress, L. Ott and H. Vogel, *J. Mol. Catal. A: Chem.*, 2005, **239**, 151–157.
- 23 L. Kong, G. Li, H. Wang, W. He and F. Ling, *J. Chem. Technol. Biotechnol.*, 2008, **83**, 383–388.
- 24 Y. Shen, S. Zhang, H. Li, Y. Ren and H. Liu, *Chem. – Eur. J.*, 2010, **16**, 7368–7371.
- 25 R. Garcia, M. Besson and P. Gallezot, *Appl. Catal., A*, 1995, **127**, 165–176.
- 26 M. Besson and P.; Gallezot, *Catal. Today*, 2000, **57**, 127–141.
- 27 F. Porta and L. Prati, *J. Catal.*, 2004, **224**, 397–403.
- 28 C. L. Bianchi, P. Canton, N. Dimitratos, F. Porta and L. Prati, *Catal. Today*, 2005, **102–103**, 203–212.
- 29 S. Demirel-Gülen, M. Lucas and P. Claus, *Catal. Today*, 2005, **102–103**, 166–172.
- 30 S. Carrettin, P. McMorn, P. Johnston, K. Griffin and G. J. Hutchings, *Chem. Commun.*, 2002, 696–697.
- 31 S. Lux and M. Siebenhofer, *Catal. Sci. Technol.*, 2013, **3**, 1380–1385.
- 32 T. Okuyama, K. Kimura and T. Fueno, *Bull. Chem. Soc. Jpn.*, 1982, **55**, 2285–2286.
- 33 A. Takagaki, J. C. Jung and S. Hayashi, *RSC Adv.*, 2014, **4**, 43785–43791.
- 34 M. Morales, P. Y. Dapsens, I. Giovinazzo, J. Witte, C. Mondelli, S. Papadokonstantakis, K. Hungerbühler and J. Perez-Ramírez, *Energy Environ. Sci.*, 2015, **8**, 558–567.
- 35 S. Bolado, R. E. Treviño, M. García-Cubero and G. González-Benito, *Catal. Commun.*, 2010, **12**, 122–126.
- 36 Z. Huang, F. Cui, H. Kang, J. Chen and C. Xia, *Appl. Catal., A*, 2009, **366**, 288–298.
- 37 H. H. C. M. Pinxt, B. F. M. Kuster and G. B. Marin, *Appl. Catal., A*, 2000, **19**, 45–54.
- 38 A. K. Kinage, P. P. Upare, P. Kasinathan, Y. K. Hwang and J.-S. Chang, *Catal. Commun.*, 2010, **11**, 620–623.
- 39 E. M. Albuquerque, L. E. P. Borges and M. A. Fraga, *J. Mol. Catal. A*, 2015, **400**, 64–70.
- 40 K. Ebitani, K. Motokura, K. Mori, T. Mizugaki and K. Kaneda, *J. Org. Chem.*, 2006, **71**, 5440–5447.
- 41 Z. P. Xu, G. S. Stevenson, C.-Q. Lu, G. Q. Lu, P. F. Barlett and P. P. Gray, *J. Am. Chem. Soc.*, 2006, **128**, 36–37.
- 42 F. Cavani, F. Trifiró and A. Vaccari, *Catal. Today*, 1991, **11**, 173–301.
- 43 T. Kameda, Y. Fubasami, N. Uchiyama and T. Yoshioka, *Thermochim. Acta*, 2010, **499**, 106–110.
- 44 M. Wang, W. J. Bao, J. Wang, K. Wang, J.-J. Xu, H.-J. Chen and X.-H. Xia, *Nature*, 2014, **4**, n. 6606.
- 45 M.-Q. Zhao, Q. Zhang, J.-Q. Huang, G.-L. Tian, J.-Q. Nie, H.-J. Peng and F. Wei, *Nat. Commun.*, 2014, **5**, n. 3410.
- 46 C. R. Gordijo, V. R. L. Constantino and D. O. Silva, *J. Solid State Chem.*, 2007, **180**, 1967–1976.
- 47 A. O. Menezes, P. S. Silva, E. P. Hernández, L. E. P. Borges and M. A. Fraga, *Langmuir*, 2010, **26**, 3382–3387.